J Mater Sci (2008) 43:3625–3637
DOI 10.1007/s10853-008-2578-1

Species variation in PrP^{Sc} protofibril models

Alexander D. Scouras · Valerie Daggett

Received: 6 March 2007 / Accepted: 23 May 2007 / Published online: 18 March 2008

Abstract The misfolding and aggregation of the prion protein (PrP) is the primary cause of a group of infectious neurodegenerative diseases including Creutzfeldt-Jacob disease in humans and Bovine Spongiform Encephalopathy in cows. A single disease can exhibit different infectious strains distinguishable by incubation time and morphology or distribution of the aggregates. Infected brain tissue from one species can be used to infect other species, but with different efficiencies, suggesting a spectrum of species compatibility. If PrP is, as widely believed, the sole component of infection, then the species and strain differences must be accounted for by the structure of the aggregates, likely influenced by each species' PrP sequence. As there are no high-resolution data exploring this hypothesis, we performed molecular dynamics simulations of PrP for human, bovine, hamster, and D147N mutant hamster sequences at low pH to induce misfolding of the protein. We selected representative converted structures from each of the four sequences and, with the guidance of experimental data, constructed models of the infectious aggregates. Both hamster monomers showed high flexibility during conversion, suggesting hamster may more easily adopt altered conformations, which in turn may explain why it is more easily infected by some other species. Human and bovine aggregates were similar, with monomers docking in $P3_1$ symmetry to form a left-handed spiral. In contrast, hamster aggregates formed a $P3_1$ right-handed spiral. We detail the differences in the converted monomers that give rise to this difference and show that our results compare favorably with experimental data.

This paper is part of the special Journal of Materials Science issue *Nano- and micromechanical properties of hierarchical biological materials: Linking mechanics, chemistry and biology; Guest Editor: Markus J. Buehler* that appeared in Journal of Materials Science volume 42, issue 21, November 2007. This paper was delayed for nonscientific reasons.

A. D. Scouras · V. Daggett
Department of Biochemistry, University of Washington, Seattle, WA 98195, USA

V. Daggett (✉)
Department of Bioengineering, University of Washington, Seattle, WA 98195-5013, USA
e-mail: daggett@u.washington.edu

Introduction

Conformational changes in the prion protein (PrP) are implicated in transmissible spongiform encephalopathy in a variety of mammalian species including Creutzfeldt-Jacob Disease (CJD), kuru, Gerstmann–Straussler–Scheinker Syndrome (GSS), and fatal familial insomnia (FFI) in humans, bovine spongiform encephalopathy (BSE) in bovines, and scrapie in sheep. The diseases share the spongiform degeneration of the central nervous system and, in many but not all cases, deposition of protein plaques comprised primarily of PrP in the affected areas of the brain [1]. Each disease has a distinct phenotype resulting from the differential localization of neurodegeneration correlating to the deposition of plaques [2]. The misfolding of cellular PrP (PrP^C) to a disease-associated state (PrP^{Sc}) and subsequent aggregation of this protein causes these diseases. These aggregates then autocatalytically misfold and aggregate further PrP^C. The prion diseases are unique in having a triple etiology of sporadic, genetic, and infectious causes—PrP^{Sc} can misfold randomly, sometimes exacerbated by genetic mutations in the PrP gene, or foreign PrP^{Sc} can be introduced to the body and begin recruiting the host's PrP^C, as in the case of ingestion of BSE-infected beef [1]. The protein-only hypothesis posits that this behavior is

completely accounted for by the biochemistry of the prion protein itself, though some debate continues [3, 4].

Protein history

In humans, the prion gene codes for a 253-residue pre-protein. Cleavage of the 22-residue N-terminal ER localization signal and a 23-residue C-terminal GPI anchor signal leaves a 208-residue protein. The first third of the protein is unstructured; a C-terminal domain starts around residue 121 and contains three α-helices (HA, HB, and HC) and a short two-stranded β-sheet (S1 and S2). PrP can be un-, mono-, or di-glycosylated at Asn181 and Asn198. Cys179 and Cys214 form a disulfide bridge between the second and third helices in both PrP^{C} and PrP^{Sc}. The GPI anchor and an N-terminal signal sequence cause the protein to localize to lipid rafts in the plasma membrane [5]. PrP^{C}'s function remains elusive, but it is currently implicated in copper-regulation [6], long-term memory [7], signaling [8], and cell death [9]. PrP^{Sc} toxicity is a result of a gain of function of the aggregates: PrP knockout mice show little phenotype besides reduced neuronal copper [10], and are immune to PrP^{Sc} infection [11]. The N-terminus up to residue 90 is proteolytically cleaved from PrP^{Sc}; the remaining fragment is protease resistant. PrP can be misfolded in the lab by high concentration of protein combined with any of a variety of denaturing conditions including high temperature, low pH, mutations, or chemical denaturant. In vivo cause(s) and even cellular location of misfolding are still under investigation, with roles suggested for endosomes, exosomes, the plasma membrane, clathrin-coated pits, caveolae, and the cytosol [12].

The NMR structures of PrP^{C} from several species have been solved [13–15], but no high-resolution data exist for PrP^{Sc} due to problems with aggregation, insolubility, and heterogeneity [16]. PrP^{Sc} aggregates in a hierarchical manner, starting with a transient misfolded monomer that oligomerizes into protofibrils. Under many conditions these further layer onto each other into fibrils, which, in turn, associate into plaques. The toxic and infectious particles may be separate species, but both occur in the soluble oligomer phase of aggregation; fibrils and plaques are relatively inert [17]. Data suggest there are multiple pathways of misfolding, only one of which leads to fibrils [18, 19]. The roles of the different pathways in disease have not been characterized.

Electron microscopy of a two-dimensional crystal found a PrP^{Sc} protofibril species that was trimeric, a diameter of <69 Å, with the glycans on the outside of the protofibril [20]. While the protofibril species is linked to infectivity and toxicity, most aggregate data have been collected on mature fibrils. Circular dichroism (CD) and fourier transform infrared spectroscopy (FTIR) reveal that PrP^{Sc} fibrils have increased extended structure and decreased α-helix relative to PrP^{C} [21–24]. X-ray diffraction studies of PrP fibrils show a cross-β structure: β-sheets with strands oriented perpendicular to the fibril axis and extending up the axis with a spacing of 4.72 Å between strands and 8.82 Å between sheets, though both meridional and equatorial reflections are diffuse, indicating some disorder [25]. The Eisenberg lab recently found that peptides extracted from PrP and 12 other amyloidogenic proteins crystallized into dry, steric zippers [26]. Recent atomic force microscopy (AFM) studies of fibrils measure the smallest fibril as 23.9 Å deep, 178 Å wide, and propagating indefinitely. These ribbons could stack up to 108.5 Å deep by 272 Å wide, with volumetric analysis indicating that monomers in a fibril occupy a space of approximately 155 Å $\times$ 18 Å $\times$ 12 Å [27]. These dimensions differ dramatically from that in the electron microscopy of the protofibrils, possibly because they represent different oligomeric species or because further conformational change is necessary in the conversion from protofibril to fibril.

Material properties of amyloid fibrils

Prion disease is a form of amyloid disease—such as Alzheimer's disease or Parkinson's disease—generally defined as the misfolding and aggregation of a protein as described above, though with a different protein and pathology in each disease. Aside from a disease or biochemical standpoint, the aggregates of amyloid diseases have gained interest from material scientists for purposes similar to carbon nanotubes [28, 29]. Protein bionanotubes are attractive because amino acid side chains (natural or not) can perform a wider variety of chemistry than carbon nanotubes and are easily manipulated in self-assembling peptides. The Lindquist group has already generated conductive amyloid fibrils [30]. Amyloid structures have other surprising properties. PrP^{Sc} retains some infectivity even after 15 min at 600 °C [31]. Insulin fibrils are as strong as steel (strength of 0.6 GPa) and as flexible as silk (stiffness of 3.3 GPa) [32]. Further studies have begun to elucidate rules controlling the propagation and shape of fibrils in peptide models [28].

Prion strains and the species barrier

For a long time farmers and scientists have noted the existence of different "strains" of prion disease in their sheep, cattle, and animal models. The differences manifest in phenotype, time until onset of disease, morphology of the aggregates, and distribution of the aggregates in the brain [33]. Assuming prion diseases are caused entirely by prion proteins of identical covalent structure, the differences between strains must be in the conformation of the protein or its aggregates. Prion disease is often difficult to transmit between species, the so-called "species barrier," indicating incompatibilities in PrP^{Sc} conformation at the

species level. Weissmann and others suggest that differences in the prion protein sequence affect the conformational space available to that species and thus the potential for interspecies infection [16].

In earlier publications we have advanced a model of the protofibril conformations of prion protein that we call the "spiral model" [34–36]. The converted monomer was generated by a molecular dynamics (MD) simulation of Hamster PrP with a D147N mutation at low pH and the protofibril was built guided by several lines of experimental evidence. This model agrees with a variety of data including exposing known epitope targets, explaining inhibitory peptides, and matching the dimensions of the 2D crystal electron microscopy data. Here we expand this model to human and bovine structures as well as providing a second example of a hamster conversion, this time with the wild-type sequence. This modeling produced surprisingly different aggregates in human and bovine as compared to hamster and also differences between the two hamster conversions, suggesting a basis of strain and species separation in prion protein.

Methods

Molecular mechanics calculations were performed using the program *in lucem* molecular mechanics (*il*mm) [37], which implements the Levitt et al. force field [38, 39] and the microcanonical ensemble (NVE). Simulations were performed with all atoms explicitly present for both protein and solvent at 298 K using a force-shifted non-bonded cutoff of 10 Å with a 2-femtosecond time step. The disulfide bond was left intact. Proteins were solvated with pre-equilibriated water boxes to a depth of 10 Å from any protein atom; waters closer than 1.9 Å to any protein atom were removed. Conversion was induced by low pH by protonating histidine, aspartate, and glutamate side chains; controls were run at neutral pH.

The initial structure for the hamster simulation, spanning residues 109–219, was provided by T.L. James and S. Farr-Jones [13]. The human structure started from residues 125–219 of NMR 1QLX [15] with residues 109–124 modeled on from the hamster structure. For bovine, the 1DWY NMR structure [14] was the base, which contains residues 124–227; residues 109–123 were modeled on from the hamster structure and the Met112Val mutation was performed in PyMOL [40]. In this case HC was left intact for a structure composed of residues 109–227. Figure 1 shows each sequence and Fig. 2 shows native and PrP^{Sc}-like structures generated through MD simulations.

To build models, we selected protein structures from a representative time point in one simulation of each species' ''misfolded'' ensemble. Each snapshot was chosen to be in a period of stable secondary structure, to be representative of

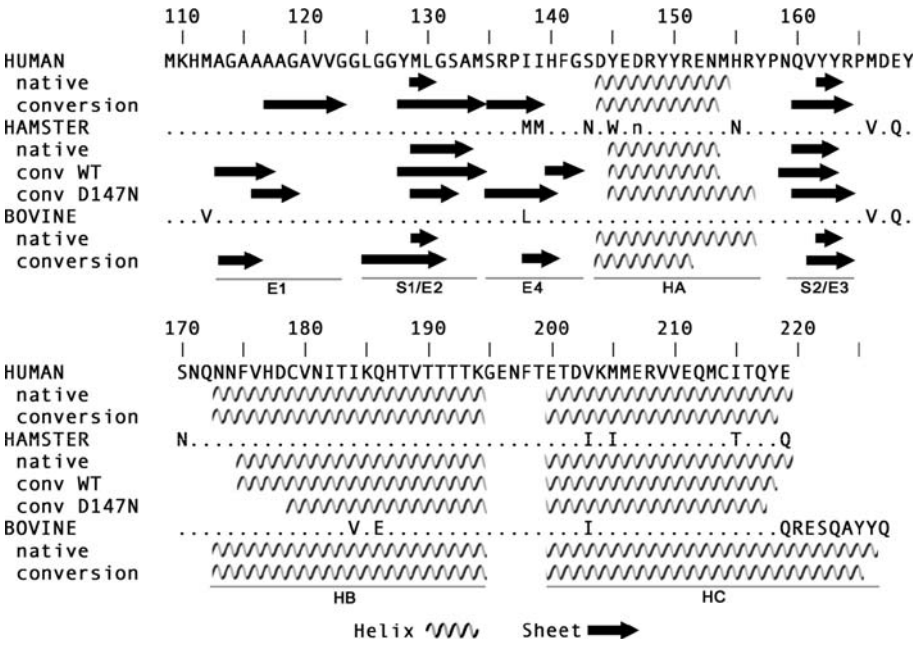

Fig. 1 Multiple sequence alignment for human, hamster, and bovine PrP. The human sequence is used for numbering. Hamster has the same numbering; bovine would start at 120. The sequence is given on the HUMAN, HAMSTER, and BOVINE lines with human as the consensus sequence and hamster and bovine only showing mutations; identical residues are indicated by a period. The lower case 'n' indicates the location of the D147N mutation in the sequence. Below each sequence is the secondary structure for the native NMR structure and converted structure from a snapshot of a low pH simulation. The simulated region is shown, so bovine runs eight residues longer than the other sequences. The labels for each secondary structure element are also given

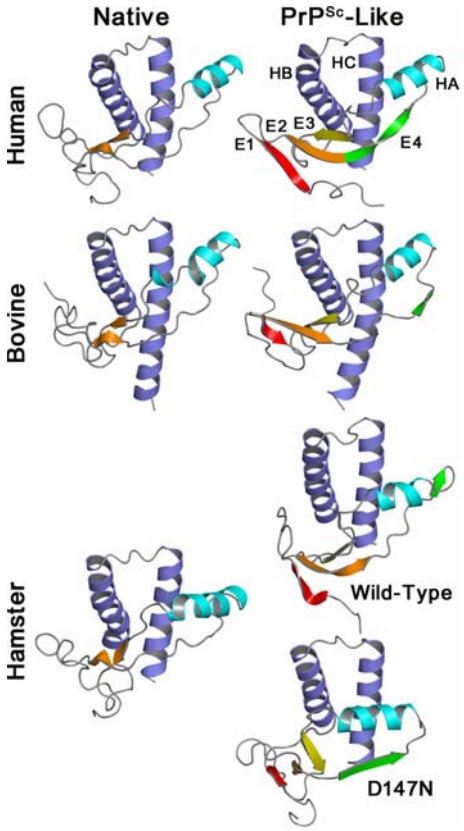

Fig. 2 PrP^{C} and MD-generated PrP^{Sc}-like structures**.** All structures are aligned via the reference frame discussed in the Methods section, then tilted forward and clockwise around HC to give the best view of the secondary structure. WT and D147N mutant hamster simulations share a starting structure with the difference of the point mutation. In hamster PrP^{C}, HA is lower and the loop before HA (residues 138–139) appears more straight than either human or bovine and HB is kinked. During conversion, HA moves more in the hamsters. All proteins have an extra strand (E1) dock onto the native sheet and an elongation in the E2-HA loop. In the D147N hamster simulation the sheet rotates counterclockwise; for wild type the sheet itself moves downward. HA is cyan, HB and HC are blue. The sheets are orange in the native structures; E1 is red, E2 is orange, E3 is yellow, and E4 is green in converted structures. This color scheme is used throughout the manuscript. The secondary structural elements are explicitly labeled for the human conversion structure for convenience

converted structures for that species, and to be free of loops or bulges interfering with potential oligomerization. For hamster, 10 low pH conversion and three control simulations were run to at least 21 nanoseconds each. The conversion structure was a 45 ns snapshot from an 80 ns simulation. Our human ensemble consists of three conversion and three control simulations extended to at least 11 ns each; we selected the 8.5 ns from a 21 ns simulation. Finally, bovine has three conversion and three control simulations run to at least 11 ns each; we selected an 18 ns structure from a 31 ns simulation. A total of 0.8 μs of simulation were performed.

Secondary structure was analyzed by using an implementation of the Dictionary of Secondary Structure of Proteins (DSSP) [41], which detects main-chain hydrogen bonding patterns, and by examination of Φ/Ψ space. In each simulation, two new strands developed; we renamed the strands E1–E4 (Fig. 2). In addition to standard α-helices and β-sheets, we found a secondary structural element called α-sheet [42]. We extended the DSSP algorithm for the detection of this high contact order α-structure by adding new bridge definitions, shown below. High contact order α-structure is placed after 3–10, α-, and π-helices in precedence so as not to override them, as helices would otherwise be detected as parallel α-sheets. In the notation below, there is a bridge between residues i and j if the h-bond criteria are satisfied, where Hbond(i,j) means there is a polar contact between the C=O of residue i and N–H of residue j with an energy of less than −0.5 kcal/mol. As with β-structure, α-ladders and α-sheets were constructed from consecutive bridges of identical type.

$$\begin{aligned}&\text{Parallel Alpha Bridge}\ (\mathrm{i},\ \mathrm{j})\\&= [\mathrm{Hbond}(\mathrm{i}-1,\ \mathrm{j}-1)\ \text{and}\ \mathrm{Hbond}(\mathrm{i},\ \mathrm{j})]\ \text{or}\\&\quad [\mathrm{Hbond}(\mathrm{j}-1,\ \mathrm{i}-1)\ \text{and}\ \mathrm{Hbond}(\mathrm{j},\ \mathrm{i})]\end{aligned}$$

$$\begin{aligned}&\text{Antiparallel Alpha Bridge}\ (\mathrm{i},\ \mathrm{j})\\&= [\mathrm{Hbond}(\mathrm{i},\ \mathrm{j}-1)\ \text{and}\ \mathrm{Hbond}(\mathrm{i}-1,\ \mathrm{j})]\ \text{or}\\&\quad [\mathrm{Hbond}(\mathrm{j},\ \mathrm{i}-1)\ \text{and}\ \mathrm{Hbond}(\mathrm{j}-1,\ \mathrm{i})]\end{aligned}$$

Monomer geometry was evaluated at 10 picosecond intervals for two nanoseconds surrounding each conversion snapshot by approximating strands E1 and E4 as lines and applying simple analytic geometry. The approximations were made on the N–Cα–C main-chain atoms in each strand: taking the first principal component as the direction vector passing through the center of mass of each line. The angle and skew distance between the lines was calculated. The "in plane" distance is the distance between centers of mass if the lines were translated so as to intersect, or the square root of the total distance squared minus the skew distance squared. These calculations and the histograms (Fig. 3) were performed and created in Mathematica [43].

Spiral models (discussed below) were built by manual rigid-body docking assuming $P3_1$ symmetry and optimizing the binding between the E4 strand of one monomer and the E1 strand of the next monomer. Larger symmetries were tried, but they left large gaps in the middle of the protofibril axis and would not fit the dimensions of the 2D EM data. These two goals alone determine the handedness, rise, and radius of the spiral as well as the packing of the converted monomer in the protofibril. In this way, hexamers were constructed. The packing was accomplished without creating steric clashes

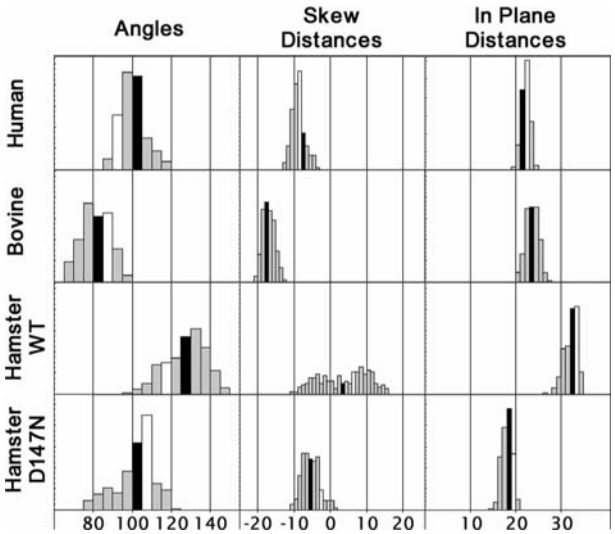

Fig. 3 Histograms of E1–E4 geometry. E1 and E4 were approximated with lines and centers of mass and their approximate geometry was calculated over an interval of two nanoseconds centered on the representative snapshot. Angles are binned at 5° and distances are binned at 1 Å. The black bar is the mean of each histogram and the white bar is the representative snapshot, if different from the mean. All histograms in a column are normalized to have equal area. Exact numbers can be found in Table 1

and without adjusting atomic coordinates of individual monomer atoms.

For purposes of analyzing the geometry of the protein, intuitive reference frames for both monomer and protofibril are needed. For the monomer, we selected three points in a stable region of the protein encompassing HB and HC, which are held together by a five-residue loop and a disulfide bridge between Cys179 towards the N-terminus of HB and Cys214 at the midpoint of HC. The Cα atom of Cys214 is defined as the primary reference, the Cα atom of Thr219 at the top of HC as the secondary reference, and the Cα atom of Cys179 as the tertiary point (Fig. 4a, b). This reference frame corresponds to the orientation of Helix C. For protofibrils, the reference frame is the fibril axis, a vector normal to the fibril axis through Cys214 of a reference monomer, and a vector orthogonal to these. Monomer packing in the protofibril is measured as the difference between the monomer reference space and the protofibril reference space and recorded as shift (the distance from the protofibril axis to Cys214), pitch (the angle HC leans out from the protofibril axis), roll (rotation normal to the protofibril axis), and yaw (the rotation of the monomer around HC).

All protein images were rendered in PyMOL from Delano Scientific [40]. Angles and distances of protofibril geometry were also calculated using the measurement tools in PyMOL. Analyses were performed using *il*mm, Perl [44] and R [45].

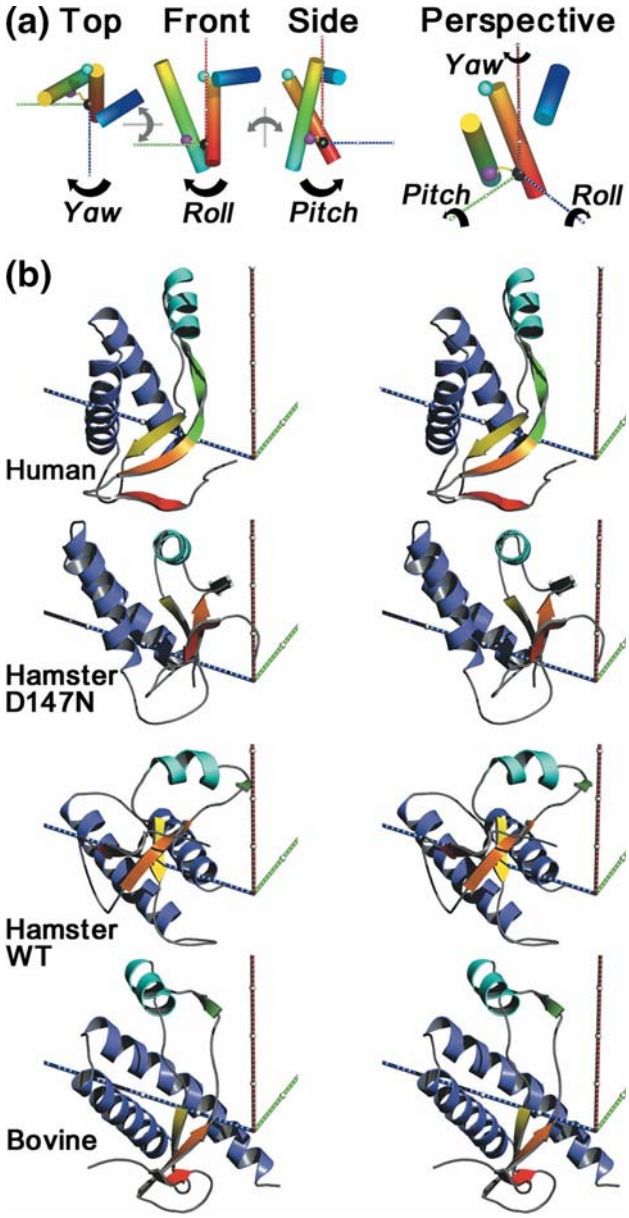

Fig. 4 Schematic and stereo view of monomer packing into protofibrils. (**a**) This reduced representation illustrates the pitch, roll, and yaw of the human conversion structure. Helices A, B, and C are colored in rainbow from blue to red. The spheres indicate the α-carbons for the three reference residues: magenta for Cys179, cyan for Thr199, and black for Cys214. Yaw is measured as the angular deviation of the green axis from a line from Cys179 to Cys214 from a top view projection. Roll and pitch are measured as the deviation from the red axis to the line between Thr199 to Cys 214 from front and side projections, respectively. (**b**) These are perspective stereo-views of monomers packed into a protofibril. The axes are the protofibril reference frame seen in Figs. 5 and 6. The blue axis passes through the Cα of Cys214 of each monomer. White balls mark every 10 Å along each axis. Each monomer has different pitch, roll, and yaw relative to the protofibril axis, positioning E1 and E4 in similar locations to connect to the next monomer. Thus, the orientation of the sheet structure relative to the monomer determines the monomer orientation in the protofibril

The sequences were retrieved from NCBI (http://www.ncbi.nlm.nih.gov/entrez/query.fcgi?db=Protein) and aligned using ClustalW [46].

Conversion of PrP^{Sc} in monomers

Sequence comparison and simulated fragments

The human and WT hamster sequences simulated correspond to the original D147N hamster conversion fragment: residues 109–219, totaling 111 residues in length (Fig. 1). The bovine sequence is slightly longer: residues 109–227, 119 residues in length. The secondary structure compositions below are calculated over the length of each simulated fragment. The sequences of these species are quite comparable. Over the 109–219 fragment, bovine and human are 93% identical (7 mutations) and human and hamster match 89% (12 mutations); bovine and hamster match 90% (11 mutations). The few mutations that do exist are mostly conservative hydrophobic changes or E/Q swaps. According to our model, many of these mutations may affect species barriers due to their proximity to the strands, especially residue 112 (a known human polymorphism) near E1 and residues 138, 139, 143, and 145 near E4. Residues 138 and 139 have shown particular involvement in the species barrier between hamster and human in an Y145Stop prion mutant [47, 48]. The potential sequence determinants of the species barriers are discussed further below.

Secondary structure

In the absence of high-resolution structural data, secondary structure composition is the primary marker of the transition from PrP^{C} to PrP^{Sc}. As experimentally determined by CD and IR spectra of a longer construct (residues 90–228), helical structure decreases from 43–47% to 17–30% and extended structure increases from 3% to 43–54% upon conversion [21, 23, 24]. For our calculations, residues are in the extended conformation if they are assigned to a sheet structure or fall into the extended region of (Φ/Ψ) space (defined broadly as Φ between -180 and 0 or 90 and 180, Ψ between -180 and -135 or 135 and 180); helical structure is as assigned by DSSP, which is based on repeating main-chain hydrogen bonding patterns. All secondary structure and geometric data are detailed in Table 1.

In our original spiral model, referred to here as the D147N hamster simulation, HB frayed while HA and HC remained stable. This, in combination with the loss of the residual N-terminal helix, was sufficient to push the model down to 33% helix extrapolated to residues 90–230, close to experimental values. The three native helices in all three new conversion simulations have remained quite stable, losing only a residue or two at the selected time point, and thus they contain slightly more helical structure than the original spiral model or experiment. The extended structure increases to 33%, including extension of the native sheet, the docking of a new strand (E1) onto that sheet, and the elongation to a strand-like conformation of the loop before HA, which we dub E4 (Fig. 2). E4 remains undocked in the monomer, but in our protofibril model it docks to E1 of a second monomer, discussed later.

The human converted structure contains 33% extended structure (37 residues: 23 sheet, 14 extended) and 48% (53 residues) helical structure over 111 residues. E1 of this structure docks to E2 with a low contact order—only three residues in the intervening loop. E4 extends three residues earlier in the sequence than in other simulations, so much so that it touches and may overlap E2. In this case, strands E2 and E4 are labels of convenience and no residues are counted more than once towards total sheet content.

The WT hamster converted structure contained 33% extended structure (37 residues: 23 sheet, 14 extended) and 44% (49 residues) helical structure over 111 residues. In this structure there is a larger, nine-residue loop between E1 and E2, leaving only four residues between E1 and the N-terminus. Three residues of α-sheet (elaborated below) formed in each of strands E1 and E4. For now we only count three residues towards the sheet content in E4, though we expect the sheet to extend along E1 in the protofibril, possibly with a mixture of α- and β-sheet.

Bovine showed 27% (32 residues: 18 sheet, 14 extended) extended structure across its full 119 residues; it had 52% (62 residues) helical content. Here there is an eight-residue loop from E1 to E2 with E1 docked in a parallel orientation to E2, causing an antiparallel E1–E4 connection. Other models have antiparallel E1–E2 and parallel E1–E4 connections.

Mobility of the structured domain and global topology

Hamster had the most mobile structured domain. This can be seen using Cα RMSD over residues 128–219 (starting at E2, neglecting the N-terminus). Comparing converted to starting structures (Table 1), hamsters deviate about twice as much as human or bovine. Further, human and bovine converted structures remain similar to each other with WT hamster and D147N hamster showing increasing deviation (Table 2). The variability in the docking of E1 can override this similarity, though. In comparison to starting structures, the hamster still differs the most, but human and bovine drastically increase. Across species, bovine is now the outlier because of its parallel-docked E1. Finally, if only the structured domain and E1 is considered, including reversing

Table 1 Properties of conversion structures and protofibril models

	Human (Å)	Bovine (Å)	Hamster WT (Å)	Hamster D147N (Å)
Converted monomer conformation				
Mutations	WT	WT	WT	D147N
Fragment	109–219	109–227	109–219	109–219
Length	111 residues	119 residues	111 residues	111 residues
Cα RMSD 128–219 (Å)	1.7	2.1	3.9	4.1
Cα RMSD whole (Å)	3.4	3.4	4.6	4.8
α Helix residues	HA: 144–153	HA: 144–152	HA: 145–153	HA: 145–156
	HB: 172–194	HB: 172–194	HB: 174–194	HB: 178–194
	HC: 200–218	HC: 200–225	HC: 200–218	HC: 200–217
	Total: 52 (47%)	Total: 59 (50%)	Total: 48 (43%)	Total: 47 (42%)
α, β Sheet residues	E1: 117–122	E1: 113–116	E1 = 113–117	E1: 116–119
	E2: 128–134	E2: 125–131	E2 = 128–134	E2: 129–132
	E3: 159–163	E3: 161–164	E3 = 159–163	E3: 160–164
	E4: 135–139	E4: 138–140	E4 = 140–142	E4: 135–140
	Total: 23	Total: 18	Total: 20	Total: 19
Other extended residues	110, 112, 116, 140, 143, 154, 157, 158, 164, 165, 166, 171, 196, 199	108, 119, 123, 132, 137, 143, 158, 160, 165, 169, 171, 198, 199, 226	112, 120, 122, 123, 137, 138, 139, 157, 158, 164, 166, 168, 170, 199	114, 115, 120, 121, 122, 125, 126, 127, 133, 143, 157, 158, 159, 165, 172, 174, 198, 199
	Total: 14	Total: 14	Total: 14	Total: 18
Total extended	37 (33%)	32 (27%)	34 (31%)	37 (33%)
E1–E4 angle [Mean ± SD (actual)]	100 ± 6 (91)	81 ± 7 (87)	127 ± 10 (119)	102 ± 10 (109)
E1–E4 skew distance	−8.7 ± 1.8 (−9.7)	−16.9 ± 1.6 (−18.3)	3.7 ± 6.7 (7.9)	−5.4 ± 2.4 (−2.4)
E1–E4 in plane distance	22.2 ± 0.9 (22.0)	23.6 ± 1.4 (23.8)	32.2 ± 1.4 (33.4)	18.0 ± 1.1 (19.2)
Monomer packing in protofibril				
Shift (Cys 214) (Å)	18	12	13	19
Shift (Center of Mass) (Å)	19	16	17	19
Pitch	25°	46°	113°	59°
Roll	−3°	−19°	44°	24°
Yaw	26°	16°	20°	14°
Protofibril geometry				
Handedness	Left	Left	Right	Right
Rise (Å)	39	39	29	29
Core diameter (Å)	40	42	43	35
Protein diameter (Å)	68	70	80	65

the direction of E1 in bovine in the alignment, deviation near the level for only residues 128–219 is achieved.

As mentioned above, the secondary structure composition of HA is barely perturbed in each of the simulations. However, there was rigid body motion of the helix in each case, which may prove critical to understanding conversion (Fig. 2). The human HA deviated least from its starting structure with a 4 Å shift towards its C-terminus with a small accommodating shift in the first three residues of the connecting loops. The bovine HA made a similar 4 Å shift in the direction of its C-terminus, but this shift propagated down the main-chain to a 2.8 Å movement in residue Ser132 in E2. WT hamster HA, in contrast, moved dramatically with a 5 Å shift towards the C-terminus of HA coupled with a 3.5 Å shift down towards the C-terminus of HC. This movement was part of a general downward shift in almost every other residue in the first half of the protein up to residue 172 at the N-terminus of HB. This is similar to the D147N hamster simulation where HA dropped 4.3 Å and moved left 6.1 Å, which also affected the structure of its sheets.

Geometry of the sheets

The β-sheets dropped 9.6 Å in the WT hamster conversion as measured at the Cα of residue 160, placing it about

Table 2 Cross species Cα-RMSD

	Bovine (Å)	WT Hamster (Å)	D147N Hamster (Å)
Cross species Cα-RMSD for residues 128–219			
Human	2.1	3.4	4.9
Bovine		3.8	4.8
WT Hamster			4.8
Cross species Cα-RMSD for residues 109–219			
Human	6.6	4.3	5.3
Bovine		7.9	7.2
WT Hamster			5.5
Cross species Cα-RMSD for E1 and residues 128–219			
Human	2.4	4.1	5.3
Bovine		4.4	5.1
WT Hamster			4.9

3.5 Å below Cys214 (Figs. 2, 4b). The sheet slopes downward at ~35° below the axis. In contrast, human and bovine start about 2 Å above Cys214 and slope down more gently, around 10° below the axis. The human and bovine E2 and E3 strands overlap almost perfectly both with each other and with their starting structures, as reflected in their low Cα RMSDs to their respective PrP^C structures. In these three converted structures, the planes of the sheets were perpendicular to the fibril axis. The shift in the D147N hamster model was large enough to rotate the strands 90° around the sheet's axis of propagation—almost parallel to the fibril axis—a large source of the Cα RMSD difference from the other species. The strands take only a slight downward slope of 10°.

E1 and E4 have a similar angle between them in all four converted structures, but the amide groups connecting to the next monomer point in different directions. The orientations of these groups determine the relative position of the next monomer. The amide groups of E1 for human and bovine point slightly down relative to HA while in both hamster conversion simulations they point out or even slightly up. E4 is just the opposite: the amide groups in the hamsters point down while in the human and bovine simulations they point out.

To further study the apparent increased flexibility of hamster PrP, we focused on the geometry of the propagation regions E1 and E4. Approximating the strands as lines, we determined their angle, skew distance, and in plane distance—the total distance subtracting the skew component—over a period of two nanoseconds centered around the representative time point. The skew "distance" is signed: a negative value indicates E4 is above E1 relative to the skew normal vector, which points up in our reference frame. Histograms (Fig. 3) and statistics (mean, standard deviation, and the representative point, in Table 1) show that the hamsters have a slightly wider angle distribution and a much wider skew distance distribution. While individual simulations have tight peaks for the in plane distance, the hamster simulations show a range of almost 15 Å, while human and bovine both center near 23 Å. The amide group orientation and skew distance are the primary determinants of strain differences in our model, as discussed below.

α-Sheet in the hamster conversion

The hamster conversion simulation resulted in a rare structural motif known as α-sheet (reviewed in [42]). Briefly, this motif is similar to β-sheet except that, in α-sheet, instead of the main-chain amide bonds alternating direction along each strand, they all point in the same direction. Our α-sheet occurs in E1 and E4, the junction between two monomers, with three residues donated from each. In our monomers, the α-strands are not stabilized by other α-strands, but instead arise from a β-bulge and an α-helix. As shown in Fig. 5, the first strand, E1, donates its carbonyl oxygens to the E1–E4 connection. It is docked onto E2 and E3, which correspond to the native β-sheet in the protein. The native sheet has a β-bulge in E2—that is there is a kink in the strands and the Gly131–Ser132 peptide bond is skipped, freeing that amide group to sync its carbonyl group with the Leu130–Gly131 peptide bond

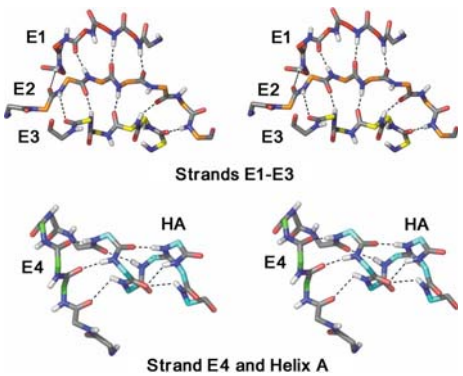

Fig. 5 Stereo view of α-sheet in Hamster WT conversion. A rare secondary structure called α-sheet formed in the Hamster WT conversion simulation. α-sheet is an extended structure similar to β-sheet except that the amide groups all face the side of a strand. Two α-strands separately formed along the interface between monomers, strands E1 and E4. E1 is in the extended β-sheet, which has bulges in it. At each bulge a residue is skipped (132 in E2 and 115 in E1) allowing the amide bond to rotate freely. This allows extra carbonyl groups to point out into solvent, creating the E1 α strand of residue 112–114. E4 is formed by docking anti-parallel onto the N-terminus of HA, creating a three-residue α strand of residues 140–142. E4 is further stabilized by the side chain of Glu146 binding to the amino group of Met139. α-Carbons are colored as in Fig. 2

before it, nucleating the α-sheet. E1 docks onto the E2 bulge, forming its own bulge, freeing the Gly114–Ala115 peptide bond. Gly114 also points its carbonyl outward, thus producing a three-residue α-strand with carbonyls free. This structure was present from 15 ns to almost 50 ns in the simulation.

E4, the amino-donating strand, is more simply docked. During conversion, HA moves towards the C-terminus of the protein while the loop preceding HA remains in roughly the same place, pushing some residues in the loop out to the side of HA. The main-chain carbonyls of these residues then dock onto the amino groups at the N-terminus of HA, but at such an angle as to retain a straight, strand-like conformation. This structure appeared after 10 ns and persisted until the end of the 80 ns simulation.

Spiral models from three species

General topology

The "spiral model" was first developed by DeMarco and Daggett [34]. Briefly, at low pH the N-terminus of the prion protein forms a new strand that docks onto the first native strand (S1). We now name the strands in this sheet E1, E2, & E3. The loop between S1 and HA elongates and we infer that this loop can form a strand, named E4. Monomers can then be docked E1 to E4 around a central axis to form a spiral with $P3_1$ symmetry. The original model was built with a structure from a low pH conversion simulation of D147N mutant of the hamster protein (here called D147N hamster). In this paper we explore models constructed with structures from human, bovine, and a wild-type hamster simulation (WT hamster) to determine the ability of the spiral model to explain the species and strain barriers found in infectious prion protein oligomers. Also, we note that this model has recently been compared extensively with experiment and with the competing β-helix model [36]. The spiral is found to be in good agreement with the available experimental information while the β-helix is at odds with many of the experimental observables.

A spiral is characterized by three parameters: handedness, rise per turn, and diameter. The WT hamster spiral is right-handed, as is the original D147N hamster model, while the bovine and human spirals are left-handed. Right-handedness means that, viewed from either end, each monomer stacks on counter-clockwise to the previous one as the protofibril elongated (Figs. 6, 7). The bovine and human spirals rise 39 Å per turn while both hamster spirals rise only 29 Å. Human, bovine, and the D147N hamster models remain fairly compact with diameters of 70, 68, and 65 Å. The WT hamster protofibril was somewhat larger at

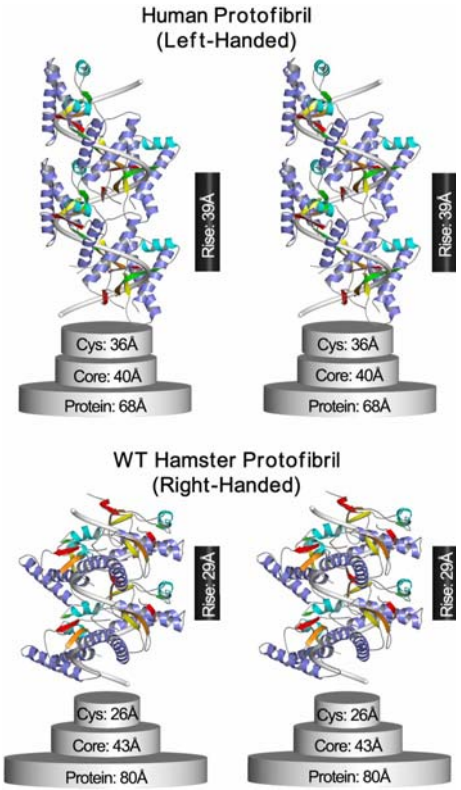

Fig. 6 Stereo protofibrils and dimensions. Human and WT hamster protofibrils are shown in a stereo-view with dimensions schematically indicated. A spiral is drawn through Cys214 of each monomer to show the connectivity of the protofibril. The black vertical bar indicates the rise between monomers. The cylinders below each model represent the diameter of various components: Cys is of the diameter encompassing the disulfide bonds; Core is the α- or β-sheet structure; Protein is the full protein, including side chains

80 Å, though all protofibrils had large enough gaps to be packed into the 69 Å space of the 2D-EM crystal [20]. The diameter of the extended α/β-sheet core is more consistent: 40 Å for human, 35 Å for D147N hamster, 43 Å for WT hamster, and 42 Å for bovine.

Monomer orientation in the protofibril models

Some properties of the geometry of the protofibril are determined by the connections between the monomers composing it; this in turn is fixed by the orientation of strands E1 and E4 to each other and to the rest of the monomer, as detailed above (Figs. 2, 6). Therefore we explored the shift, pitch, roll, and yaw of the monomer in its packing in the protofibril and compare it to the orientation of the strands. To measure the orientations, a three-point reference frame was created about HC, as discussed in the Methods section, between the α carbons of Cys 214, Thr 199, and Cys 179 (Fig. 4a). In vivo, HC terminates in the GPI anchor, embedding the protein in the plasma

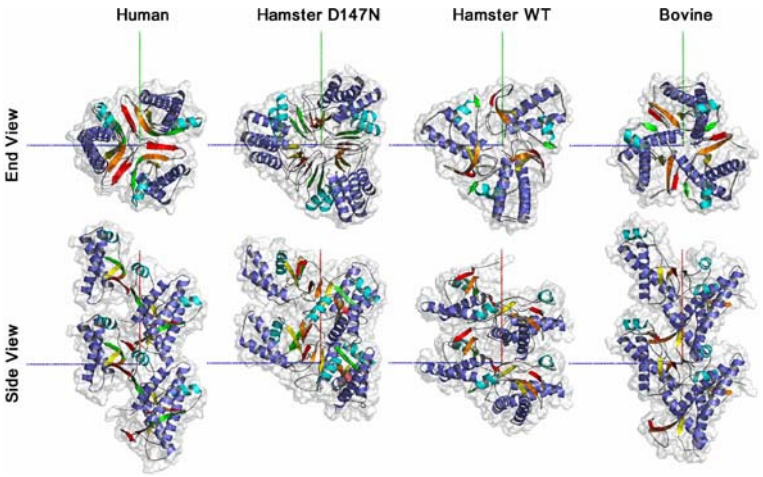

Fig. 7 End and side views of protofibril models. Hexameric spiral models were built from each of the four conversion structures. The red axis in the side view is the protofibril axis; the blue axis passes through the α-Carbon of Cys214 of the third monomer from the bottom, shown in detail in Fig. 4b; the green axis is orthogonal to these two. Each axis is 50 Å long. The figure is colored as in Fig. 2 and the surface over all atoms is included

membrane; having a pitch and roll of 0° corresponds to HC oriented normal to the membrane. For protofibril elongation happening on the surface of a membrane, these orientations may have implications for the kinetics of aggregation.

Shift is the distance from the protofibril axis to the α-carbon of Cys 214, an indication of how tightly the monomers pack, though pitch and roll influence the final diameter (Figs. 6, 7). Bovine and WT hamster pack closest at 12 Å and 13 Å, respectively. Human is further away at 18 Å, and D147N hamster model is at 19 Å. We also calculate the radius of the center of mass over residues 109–219 and find somewhat less variation: bovine at 16 Å, WT hamster at 17 Å, human at 19 Å, and D147N hamster at 19 Å. Pitch—the angle at which HC is tilted away from the protofibril axis—is the most variable rotation. Human is fairly vertical at 25° off axis, bovine leans diagonally at 46°, D147N hamster leans just a bit more at 59°, and WT hamster leans all they way back to 113°, causing the larger diameter observed for that protofibril. Roll is related to the handedness of the helix, determined by whether E1 or E4 is higher along the protofibril axis, to the extent that HA remains docked to HC. Human and bovine roll left to −3° and −19°, respectively; WT and D147N hamster models roll right to 44° and 24°. Finally, yaw determines how E1 and E4 face into the protofibril. As the distance between E1 and E4 is constrained in a given monomer, the protofibril is symmetric, and these strands must meet between monomers, we expect there to be little variance in yaw. Indeed, we find at most 12° of variance: from the most counterclockwise protein, rotating clockwise, human is 26°; WT hamster is 20°, bovine is 16°, and D147N hamster is 14°.

Despite the variations discussed above, the sheet structure remains in approximately the same orientation in the middle of the fibril. In particular, the skew normal between E1 and E4 is close to parallel to the fibril axis. This means the sign and magnitude of the skew distance have a large effect on the handedness of the spiral. If E1 is below E4 (negative skew distance), then spirals tend to be left-handed, as in bovine and human. The representative structures picked for hamsters had skew distances near or above 0, allowing them to form right-handed spirals. An important future test of our model will be building models from close intervals to determine their handedness.

Discussion

We have performed multiple MD simulations of three species of prion protein: human, bovine, WT hamster, and a D147N hamster mutant. These simulations were performed at low pH so as to induce a conformational change, resulting in increased β-sheet (and some α-sheet) in the protein, in agreement with experiment. In particular, the N-terminus of the protein forms a strand (labeled E1) that docks onto the native β-sheet and the loop before HA elongates (labeled E4), suggesting a potential strand for docking onto a separate monomer. We selected a representative conversion structure for each species with which to build protofibril models. With these snapshots and the assumption of $P3_1$ symmetry in the protofibril, we created a model of oligomerization wherein individual PrP monomers dock E1 to E4 around a protofibril axis to form a spiral. We examine the geometry of the converted structure and protofibril model of each species for implications about the strain and species barriers.

Species conformational preference

Hamster is the outlier of the three species as judged by sequence similarity (Fig. 1), the PrP^C NMR structures (Fig. 2), and converted structures. By Cα RMSD of the core residues (Tables 1, 2), hamster deviates most from its starting structure and from the converted structures of the

other species. All four conversions show a shift in HA, but the hamster structures shift about twice as far and the movement propagates to the extended structure—the human and bovine shifts are confined. Low pH eliminates stabilizing salt-bridges [49] releasing HA from HC. This movement is in the region taken directly from NMR structures and the species with modeled N-termini are more stable, so this is unlikely to be an effect of modeling. The hamster sequence prefers to point strand E1 out or up and E4 down from HA, while in human and bovine E1 points down and E4 points out from HC (Figs. 2, 4b). These results suggest hamster is more flexible, making it likely to display a broader range of strains and be more susceptible to infection from other species, but less likely to infect them.

The otherwise subtle differences in orientation of strands E1 and E4 have clear ramifications in our spiral model: pointing E1 up and E4 down and a positive skew distance produces the right-handed spiral seen in hamsters and vice versa for human and bovine. This is not a simple symmetry operation in the monomers, though—they must pack differently in the protofibril, making different contacts and exposing different residues to solvent, giving one possible basis of strain differentiation in prion diseases.

Experimental comparison

Recently, Surewicz and colleagues examined the Y145Stop mutant of the human, mouse, and hamster sequences [47, 48]. Human and mouse seed each other's aggregation but not hamster's, while hamster seeds aggregation in mouse and itself, resulting in a human–mouse compatibility grouping. They isolated the difference to residues 138 and 139—IleIle in human, MetIle in mouse, and MetMet in hamster—and confirmed the discovery with mutational studies in human and hamster. On further study, human and mouse PrP^{Sc} both had similar secondary structure by FTIR and produced ribbed fibrils while the hamster structure was different and had smooth fibrils [50]. Bovine's sequence at this location, LeuIle, is more similar to human and in our studies we find human and bovine group together with hamster as the outsider. This similarity is seen in both the monomer converted structures and in the handedness of the resulting protofibril model. Examining these residues in the NMR and conversion structures, Met139 produces a kink in the main-chain towards HC, while Ile 139 kinks away (Fig. 2). The mouse PrP NMR structure 1AG2 also correlates with the human and bovine structures. In our model, this kink is in and may affect the orientation of E4, determining the propensity for right- or left-handed protofibrils to form upon conversion. In hamster PrP, this kink causes a rotation of the top of HA away from HC by 30–45°. This rotation allows Tyr150 to reach high enough to bond to Asp202; this bond may play a role in how HA is positioned in hamster. In human, bovine, and mouse, Tyr150 is tucked under HA to bond to the main-chain carbonyl of Pro137.

From this evidence we have the correct grouping, but the wrong direction of infectivity. However, these results are from a truncation mutant terminating prior to HA—the interactions between helices have great influence over the conformations available to the protein. Earlier work by Lansbury and Caughey comparing full-length mouse and hamster PrP supports our predictions: mouse infects hamster, but is not susceptible to hamster infection [51]. This study also isolated residue 139—and additionally 155 and 170—as important in the species barrier. It is also interesting to note that hamster and "hamsterized" transgenic mice have very short incubation times after infection and so are favored animal models for studying the disease [52–54].

Spiral model accommodates full-length PrP

We constructed these models using residues 109–219 with the human and hamster simulations and 109–227 with the bovine species. PrP^{Sc} is usually found as the 90–230 fragment and our model accommodates these extra residues. For the N-terminus, we predict yet another strand to dock on the current E1, leaving any leftover residues exposed outside the protofibril so that the chain can be proteolytically cleaved around residue 90. In low pH simulations of human PrP residues 90–230, we have seen β-hairpin formation in residues 90–108 [49]. Addition of another strand would cause a minor increase in diameter in the protofibril. The C-terminus of the protein is expected by epitope studies to remain helical in conversion, as in the native structure, and the bovine model shows the full helix packing against the middle of the protofibril with room for the unstructured tail. The other models have gaps to accommodate the C-terminus. The C-terminus remains solvent exposed so is available to antibodies.

Minor differences suggest sub-strains

Despite the similarities between the conversion structures of wild type and D147N hamster sequences and right-handedness of both protofibrils, the modeled aggregate structures may still be different sub-strains of the right-handed helix strain. There are different registers in the docking of E1 to E2 and in the assignment of strand E4. The monomers pack differently, but might be able to interconvert within a protofibril. This transition seems likely to play a role when PrP^{C} of one species docks to PrP^{Sc} of another species, adapting the strain to the new species. It would not be possible to transition between

right- and left-handed strains, as the transition would involve the two monomers surrounding the transition point trying to pack into the same space.

Conclusions

We have found significant differences in converted structures between different species of the prion protein. Hamster has distinct converted monomers and protofibril structures as compared to human and bovine PrP, ultimately showing greater flexibility in its conformation space and a preference for right-handed spirals in our protofibril model. Human and bovine are more constrained and prefer left-handed spirals. This grouping correlates well with experimental data, which grouped human and mouse against hamster, isolating the difference to mutations in residues 138 and 139, where human and bovine show more similarity than to hamster. Studies of full-length PrP^{Sc} show hamster to be more susceptible to infection by mouse than the reverse, as predicted by its greater ability to adapt to conformations of different infectious strains. These findings provide more circumstantial evidence for the spiral model as the basis of oligomerization in the prion protein and suggest a mechanism of PrP strains based solely on conformational differences within the prion protein. As the data suggesting multiple orthogonal oligomerization pathways is developed, it will be interesting to see where our model fits into it, and even more interesting which of the different pathways are pathogenic. We are currently devising further simulations and experiments to test and refine these models as well as studying the initial misfolding of PrP^{C} itself.

References

1. Fornai F, Ferrucci M, Gesi M, Bandettini di Poggio A, Giorgi FS, Biagioni F, Paparelli A (2006) Brain Res Bull 69:95
2. Mead S (2006) Eur J Hum Genet 14:273
3. Griffith JS (1967) Nature 215:1043
4. Bolton DC, McKinley MP, Prusiner SB (1982) Science 218:1309
5. Walmsley AR, Zeng F, Hooper NM (2003) J Biol Chem 278:37241
6. Burns CS, Aronoff-Spencer E, Legname G, Prusiner SB, Antholine WE, Gerfen GJ, Peisach J, Millhauser GL (2003) Biochemistry 42:6794
7. Papassotiropoulos A, Wollmer MA, Aguzzi A, Hock C, Nitsch RM, de Quervain DJ (2005) Hum Mol Genet 14:2241
8. Lasmezas CI (2003) Br Med Bull 66:61
9. Sikorska B (2004) Folia Neuropathol 42(Suppl B):89
10. Brown DR, Qin K, Herms JW, Madlung A, Manson J, Strome R, Fraser PE, Kruck T, von Bohlen A, Schulz-Schaeffer W, Giese A, Westaway D, Kretzschmar H (1997) Nature 390:684
11. Bueler H, Aguzzi A, Sailer A, Greiner RA, Autenried P, Aguet M, Weissmann C (1993) Cell 73:1339
12. Campana V, Sarnataro D, Zurzolo C (2005) Trends Cell Biol 15:102
13. James TL, Liu H, Ulyanov NB, Farr-Jones S, Zhang H, Donne DG, Kaneko K, Groth D, Mehlhorn I, Prusiner SB, Cohen FE (1997) Proc Natl Acad Sci USA 94:10086
14. Lopez Garcia F, Zahn R, Riek R, Wuthrich K (2000) Proc Natl Acad Sci USA 97:8334
15. Zahn R, Liu A, Luhrs T, Riek R, von Schroetter C, Lopez Garcia F, Billeter M, Calzolai L, Wider G, Wuthrich K (2000) Proc Natl Acad Sci USA 97:145
16. Weissmann C (2005) Cell 122:165
17. Caughey B, Lansbury PT (2003) Annu Rev Neurosci 26:267
18. Baskakov IV, Legname G, Baldwin MA, Prusiner SB, Cohen FE (2002) J Biol Chem 277:21140
19. Eghiaian F, Daubenfeld T, Quenet Y, van Audenhaege M, Bouin AP, van der Rest G, Grosclaude J, Rezaei H (2007) Proc Natl Acad Sci USA 104:7414
20. Wille H, Michelitsch MD, Guenebaut V, Supattapone S, Serban A, Cohen FE, Agard DA, Prusiner SB (2002) Proc Natl Acad Sci USA 99:3563
21. Caughey BW, Dong A, Bhat KS, Ernst D, Hayes SF, Caughey WS (1991) Biochemistry 30:7672
22. Gasset M, Baldwin MA, Fletterick RJ, Prusiner SB (1993) Proc Natl Acad Sci USA 90:1
23. Pan KM, Baldwin M, Nguyen J, Gasset M, Serban A, Groth D, Mehlhorn I, Huang Z, Fletterick RJ, Cohen FE et al (1993) Proc Natl Acad Sci USA 90:10962
24. Jackson GS, Hill AF, Joseph C, Hosszu L, Power A, Waltho JP, Clarke AR, Collinge J (1999) Biochim Biophys Acta 1431:1
25. Nguyen JT, Inouye H, Baldwin MA, Fletterick RJ, Cohen FE, Prusiner SB, Kirschner DA (1995) J Mol Biol 252:412
26. Sawaya MR, Sambashivan S, Nelson R, Ivanova MI, Sievers SA, Apostol MI, Thompson MJ, Balbirnie M, Wiltzius JJ, McFarlane HT, Madsen AO, Riekel C, Eisenberg D (2007) Nature 447:453
27. Anderson M, Bocharova OV, Makarava N, Breydo L, Salnikov VV, Baskakov IV (2006) J Mol Biol 358:580
28. Zhang S (2003) Nat Biotechnol 21:1171
29. Waterhouse SH, Gerrard JA (2004) Aust J Chem 57:519
30. Scheibel T, Parthasarathy R, Sawicki G, Lin XM, Jaeger H, Lindquist SL (2003) Proc Natl Acad Sci USA 100:4527
31. Brown P, Rau EH, Johnson BK, Bacote AE, Gibbs CJ Jr, Gajdusek DC (2000) Proc Natl Acad Sci USA 97:3418
32. Smith JF, Knowles TP, Dobson CM, Macphee CE, Welland ME (2006) Proc Natl Acad Sci USA 103:15806
33. Bruce ME (2003) Br Med Bull 66:99
34. DeMarco ML, Daggett V (2004) Proc Natl Acad Sci USA 101:2293
35. DeMarco ML, Daggett V (2005) C R Biol 328:847
36. DeMarco ML, Silveira J, Caughey B, Daggett V (2006) Biochemistry 45:15573
37. Beck DAC, Alonso DOV, Daggett V (2000–2008) *In lucem* molecular mechanics. University of Washington, Seattle, WA
38. Levitt M, Hirshberg M, Sharon R, Daggett V (1995) Comput Phys Commun 91:215
39. Levitt M, Hirshberg M, Sharon R, Laidig KE, Daggett V (1997) J Phys Chem B 101:5051
40. DeLano WL (2002) 0.99rc6 ed. DeLano Scientific, San Carlos, CA, USA
41. Kabsch W, Sander C (1983) Biopolymers 22:2577
42. Daggett V (2006) Acc Chem Res 39:594
43. I. Wolfram Research (2005) Mathematica, 5.2 ed. Wolfram Research, Inc., Champaign, IL
44. T.P. Foundation (2006) 5.8.8 ed. The Perl Foundation
45. R.D.C. Team. R Foundation for Statistical Computing, Vienna Austria3-900051-07-0, 2005

46. Thompson JD, Higgins DG, Gibson TJ (1994) Nucleic Acids Res 22:4673
47. Kundu B, Maiti NR, Jones EM, Surewicz KA, Vanik DL, Surewicz WK (2003) Proc Natl Acad Sci USA 100:12069
48. Vanik DL, Surewicz KA, Surewicz WK (2004) Mol Cell 14:139
49. DeMarco ML, Daggett V (2007) Biochem 46:3045
50. Jones EM, Surewicz WK (2005) Cell 121:63
51. Kocisko DA, Priola SA, Raymond GJ, Chesebro B, Lansbury PT Jr, Caughey B (1995) Proc Natl Acad Sci USA 92:3923
52. Kimberlin RH, Marsh RF (1975) J Infect Dis 131:97
53. Marsh RF, Kimberlin RH (1975) J Infect Dis 131:104
54. Scott M, Foster D, Mirenda C, Serban D, Coufal F, Walchli M, Torchia M, Groth D, Carlson G, DeArmond SJ et al (1989) Cell 59:847